Hindawi
International Journal of Biomaterials
Volume 2023, Article ID 4602374, 11 pages
https://doi.org/10.1155/2023/4602374

Research Article

Vanadium Pentoxide Nanoparticles Doped ZnO: Physicochemical, Optical, Dielectric, and Photocatalytic Properties

Imen Massoudi,[1,2] Ridha Hamdi,[1,2] Amani Rached,[1,2] Zainah A. AlDhawi,[2,3] Fatimah M. Alobaidan,[1] Hawra M. Alhamdan,[1] Ghadeer A. Almohammed Ali,[1] Fatimah E. Almuslim,[1] and Amor Ben Ali[2,3]

[1]*Department of Physics, College of Science, Imam Abdulrahman Bin Faisal University, P.O. Box 1982, Dammam 31441, Saudi Arabia*
[2]*Basic and Applied Scientific Research Center, Imam Abdulrahman Bin Faisal University, P.O. Box 1982, Dammam 31441, Saudi Arabia*
[3]*Department of Chemistry, College of Science, Imam Abdulrahman Bin Faisal University, P.O. Box 1982, Dammam 31441, Saudi Arabia*

Correspondence should be addressed to Imen Massoudi; ismassoudi@iau.edu.sa

Received 2 September 2023; Revised 28 October 2023; Accepted 7 November 2023; Published 18 November 2023

Academic Editor: Swarup Roy

In this work, vanadium pentoxide nanoparticles (V_2O_5) derived by the chemical coprecipitation route were used to synthesize various vanadium-doped ZnO nanocomposite samples via the standard solid-state reaction process. The effect of V_2O_5 nanoparticles on the physicochemical properties of ZnO was discussed. The prepared samples were characterized by X-ray diffraction, Fourier-transform infrared spectroscopy, scanning electron microscopy combined with energy-dispersive spectroscopy, and UV-visible spectroscopy. A diffuse reflectance spectroscopic approach is described to determine the bandgap energy (Eg) of the samples. The dielectric and photocatalytic characteristics are also examined. The photocatalytic performance of the prepared materials was tested under visible light using methylene blue (MB) as a pollutant dye model. As a result, it is found that the addition of V_2O_5 enhances the photodegradation of MB. The kinetics of the photodegradation reaction was found to follow a pseudo-first-order model.

1. Introduction

Zinc oxide (ZnO), being a broad bandgap semiconductor, is a potential host for solid-state blue to UV optoelectronics, including laser development [1]. This has crucial uses in high-density data storage systems, solid-state lighting, in which white light is generated by phosphors triggered by blue or UV light-emitting diodes, secure communications, and bio-detection [2]. Transparency to visible light opens the door to the development of transparent electronics, UV optoelectronics, and integrated sensors from the same material systems. Recent advances in the quality and control of conductivity in ZnO have heightened interest in its usage for surface acoustic wave devices, gas sensors, solar cell displays, and window materials [3–7].

Photoluminescence photoconductivity, photocatalytic activities, and absorption studies of ZnO reveal the inherent direct bandgap, a strongly bound exciton state, and gap states attributable to point defects [8, 9]. The near-band-edge UV photoluminescence peak at 3.2 eV at room temperature is ascribed to an exciton state, as the exciton binding energy is around 60 meV [10]. Furthermore, visible emission is detected due to the presence of defect states. A blue-green emission has been explained in terms of transitions involving self-activated

centers formed by a doubly ionized zinc vacancy and an ionized interstitial Zn^+ [10], oxygen vacancies [11], and donor-acceptor pair recombination involving an impurity acceptor [12].

Furthermore, ZnO has excellent piezoelectric properties because of its wurtzite structure, which provides strong polarity along the c-axis direction. Several piezoelectric devices have been developed over the last few years using ZnO nanostructures and thin films, including piezoelectric nanogenerators (PENGs), film bulk acoustic resonators (FBAR), pressure sensors, piezoelectric vector hydrophones, and piezoelectric micromachined ultrasonic transducers (PMUT) [12–14].

A key parameter for evaluating piezoelectric performance is the d33 coefficient [13], for pure bulk ZnO, it is 9.9 $pm \cdot V^{-1}$. Nevertheless, an advanced piezoelectric device still requires a stronger piezo response. Doping is one of the most effective methods of improving piezoelectric properties. The use of transition metals (TMs) in ZnO nanoparticles (NPs) shows tremendous potential as a photocatalyst, sensor, optoelectronic, medical, spintronic, and piezoelectric devices [14, 15]. Indeed, the electronic structure of the host lattice is influenced by the strong hybridization of 3*d* orbitals of the transition metal ions with the *s* or *p* orbitals of the neighboring anions. This hybridization gives rise to the strong magnetic interaction between the localized 3*d* spins and the carriers in the host valence band. As a result, a giant piezo response of 3*d*-TM doped ZnO has been demonstrated in several reports; 120 $pm \cdot V^{-1}$ for Cr-doped ZnO [16], 127 $pm \cdot V^{-1}$ for Fe-doped ZnO [17], and 86 $pm \cdot V^{-1}$ for Mn-doped ZnO [18]. Among all TMs, ZnO doped with vanadium (V) produces the highest piezoelectric coefficient, 170 $pm \cdot V^{-1}$, with a vanadium doping concentration of 2.5 at% [19]. This value is comparable to perovskites, suggesting that current doped ZnO devices could be improved qualitatively and could be used in a broader variety of applications. Therefore, V-doping is more effective than other TM dopants at improving piezoelectric properties.

A number of studies have revealed that V-doped ZnO exhibits very interesting optical properties, including photoluminescence (PL) and excitation of photoluminescence (EPL) [20, 21]. Therefore, the application of this semiconductor to visible photocatalysis can be of interest. Many studies have shown that using vanadium pentaoxide (V_2O_5) as a doping element improves the host's structural and optical properties. Nevertheless, the use of doping V_2O_5 element, as a photocatalyst, is very rarely studied as it is common for vanadium to be used as junction catalysts with other oxides; supported-vanadium-oxide-catalysts, such as Al_2O_3, SiO_2, TiO_2, and ZrO_2 [22].

Herein, the effect of vanadium- (V-) doped ZnO on dielectric properties besides the photocatalytic performance of the prepared materials was studied. The prepared materials were characterized by X-ray diffraction (XRD), Fourier-transform infrared (FTIR) spectroscopy, scanning electron microscopy combined with energy-dispersive spectroscopy (SEM-EDX), and UV-visible spectroscopy. The dielectric properties of samples were studied using complex impedance spectroscopy.

2. Experimental

2.1. Synthesis of Vanadium-Doped ZnO. Vanadium- (V-) doped zinc oxide samples were prepared using a solid-state reaction. Synthetic V_2O_5 nano-powder was added to commercial nano-powder ZnO in various molar percent, then combined and mashed for 30 minutes in a high-speed ball milling (Ritsch model) equipped with MTI muffle furnaces operating at 1000 rpm. After that, the samples were compacted into pellets, placed in alumina crucibles, and heated in a furnace at 500°C for 6 hours. After cooling to room temperature, they were ground manually for 30 minutes. The obtained samples bearing the acronym 3 V, 5 V, 7 V, and 9 V for 3, 5, 7, and 9 molar percent of V_2O_5, respectively.

2.2. Characterizations. The obtained samples were structurally characterized using XRD analysis. The diffracted data were collected on an automatic diffractometer Philips Panalytical X'Pert ProMPD using a Cu Kα radiation source ($\lambda = 1.5406$ Å) in the 2θ range of 10–80°. Fourier-transform infrared spectroscopy analysis for the samples was carried out on an IRAffinity-1S from Shimadzu. The samples were vacuum dried and then analyzed with FTIR spectroscopy in the range of $4000 - 500\ cm^{-1}$ wave numbers. Scanning Electron Microscopy coupled with energy-dispersive X-ray was performed using JEOL 2010 (200 kV) microscope. UV-visible diffuse reflectance spectroscopy (UV-vis DRS) measurements were performed using an AvaSpec-2048 Fiber Optic Spectrometer with a symmetrical Czerny–Turner design. Spectra were recorded in the range of 200–1000 nm using a 2048-pixel CCD detector array. The dielectric properties of prepared materials were studied using complex impedance spectroscopy (CIS) Palmsens4 from Palmsens. The samples are pelletized with a 13 mm diameter and a 2 mm thickness and then placed between two glasses coated with conductive FTO electrodes. The complex impedance measurements were carried out at room temperature by scanning the frequency from 1 Hz to 1 MHz with a voltage of 5 m $V_{RMS.}$

2.3. Photocatalytic Performance under Visible Light. The photocatalytic performance of the prepared catalysts was evaluated by employing the degradation of methylene blue (MB) under visible light. Typically, 30 mg of the catalyst was loaded into a beaker containing 30 mL of MB solution (20 mg/L). The experiments were carried out in the dark for 40 min to achieve the adsorption-desorption equilibrium. The blank experiment (without catalyst) was also conducted under visible light to evaluate any possible direct photolysis of the dye. Photodegradation was performed using a HQI-E 400 W/n plus visible lamp and maintained under magnetic stirring >1200 rpm to overcome any external diffusion. At different time intervals, samples were drawn from the reaction medium and analyzed using a Shimadzu UV-1900 UV-vis spectrophotometer over the 200–800 nm range. The degradation efficiency was calculated using the following equation:

$$D\% = \frac{(C_0 - C_t)}{C_0} \times 100, \quad (1)$$

where C_0 and C_t represent the concentration of MB at the initial time ($t = 0$) and reaction time ($t \neq 0$), respectively.

3. Results and Discussion

3.1. X-Ray Diffraction. Figure 1 depicts the powder XRD pattern of the samples collected at room temperature. The XRD pattern reveals that a solid-state reaction has occurred by displaying a secondary phase. Compared to pure ZnO, all doped samples have a dominated hexagonal wurtzite phase and a minor orthorhombic phase assigned to Zn_3 $(VO_4)_2$ according to the JCPDS340378 card clearly shown in sample 9 V. The hexagonal wurtzite of V_2O_5 doped ZnO solid solution presents unit cell parameters $a = b = 3.253$ Å and $c = 5.213$ Å (JCPDS01089139). The orthorhombic crystalline structure of Zn_3 $(VO_4)_2$ is characterized by $a = 8.299$ Å, $b = 11.52$ Å, and $c = 6.111$ Å.

The unit cell parameter of all samples was refined via the Rietveld refinement method, (full pattern matching option) using the FULLPROF program. For clarity reasons, only 7 V sample results are presented in Figure 2. The ratability factors are $\chi^2 = 1.43$, $R_p. = 14.8$, $R_{wp}. = 21.1$, and $R_{exp}. = 17.64$. These values indicate a good agreement between the calculated and experimental data. The unit cell parameters for all samples are summarized in Table 1.

Based on the data presented in Table 1, a systematic increase of both unit cell parameters a and c with increasing the molar percent of vanadium (V) oxide. These results can be explained by comparing the ionic radii for tetrahedral coordination of Zn^{2+} (0.88 Å) and V^{2+} (0.93 Å). Hence, the substitution of zinc for vanadium in the ZnO matrix induces an expansion of unit cell volume.

The crystallite sizes "D" was calculated through either Scherrer or Williamson–Hall equations as follows:

Scherrer equation:

$$\mathbf{D} = \frac{\mathbf{k\lambda}}{\beta \mathbf{cos}\theta}, \quad (2)$$

where $k = 0.89$ is a constant, λ = 1.5406Å, θ, and β are the diffraction angle and the corresponding full width at half-maximum FWHM of the observed peak, respectively.

Williamson–Hall equation:

$$\beta \cos\theta = \frac{k\lambda}{D} + 4\varepsilon \sin\theta, \quad (3)$$

where ε is the strain of the samples.

Figure 3 depicts the variance of $\beta \cos\theta$ against $4 \sin\theta$ for all samples except sample 9 V. The full width at a half-maximum of 9 V cannot be accurately determined due to the X-ray fluorescence which is more pronounced with a high molar percent of vanadium oxide. For all samples, a small variation of strain is observed (Table 2). It may be attributed to lattice distortion due to the substitution of Zn^{2+} (0.88 Å) by vanadium V^{2+} (0.93 Å) in the zinc oxide matrix. Santi Maensiri [23] reported comparable results. The crystallite size calculated in equations (2) and (3) presents the same trend. It actually decreases with increasing vanadium molar percent. The discrepancy in D values between the Scherrer and Williamson–Hall methods can be explained by the fact that the Scherrer methodology ignores strain.

3.2. UV-Vis Diffuse Reflectance Spectroscopy. The UV-vis diffuse reflectance spectroscopy was employed in this work to investigate the energy structures and optical characteristics of V_2O_5-doped ZnO samples. Figure 4 illustrates the diffuse reflectance spectrum of prepared samples. They display a dramatic rise in reflectance at 370 nm.

The band gap energy values were evaluated using the Kubelka–Munk method. The bandgap energy (E_g) is a critical property of semiconductor materials. The value of E_g, like other physical and chemical characteristics of materials, their value may be modified by numerous aspects such as the synthesis pathway and/or processing method. In this regard, optical characterization techniques combined with the well-known Tauc method are by far the most extensively used approach for determining the E_g of supported materials [24]. It has been demonstrated that when properly conducted, this approach yields precise values of E_g [25]. The Tauc charts are created using DRS by computing the reemission function, $F(R_\infty)$:

$$F(R_\infty) = \frac{K}{S} = \frac{(1 - R_\infty)^2}{2R_\infty}, \quad (4)$$

$$F(R_\infty)\mathrm{h}\nu = \alpha \mathrm{h}\nu = C\left(\mathrm{h}\nu - E_g\right)^n, \quad (5)$$

where R_∞ is the reflectance of the sample with "infinite thickness," hence, there is no contribution of the supporting material, K, and S are the absorption and scattering K-M coefficients, respectively, C is a proportionality constant. α represents the absorption coefficient of the material, h denotes Planck's constant, ν reflects the frequency of light, hν is the energy of the incident photon, and n is a coefficient that depends on the kind of electronic transition; $n = 1/2$ for direct allowed transition, $n = 3/2$ for direct forbidden transition, $n = 2$ for indirect allowed transition, and $n = 3$ for indirect forbidden transition. In our situation $n = 1/2$: for direct transition, mode materials), because ZnO is a direct bandgap semiconductor [26]. The Tauc approach basically finds the value of E_g at the intersection of the straight-line fit of the region associated with the optical absorption edge (i.e., the Tauc segment; TS) and the hν -axis in the related $(\alpha \mathrm{h}\nu)^2$ vs. hν plot (Tauc plot) [27–29].

Through equations (4) and (5) the bandgap (E_g) is calculated by constructing a Tauc plot (Figure 5) from the reflectance spectra.

Table 3 lists the E_g values for each sample. It is found that the bandgap of V_2O_5/ZnO has little change consistently with the increasing concentration of V_2O_5. This occurs because V^{2+} ions take the place of Zn^{2+} ions in the lattice crystal, implying that V^{2+} ions contribute to the valence band of ZnO materials. These results are comparable to those encountered by previous researchers [30]. This scenario decreased Zn-O bonding while promoting V-O development.

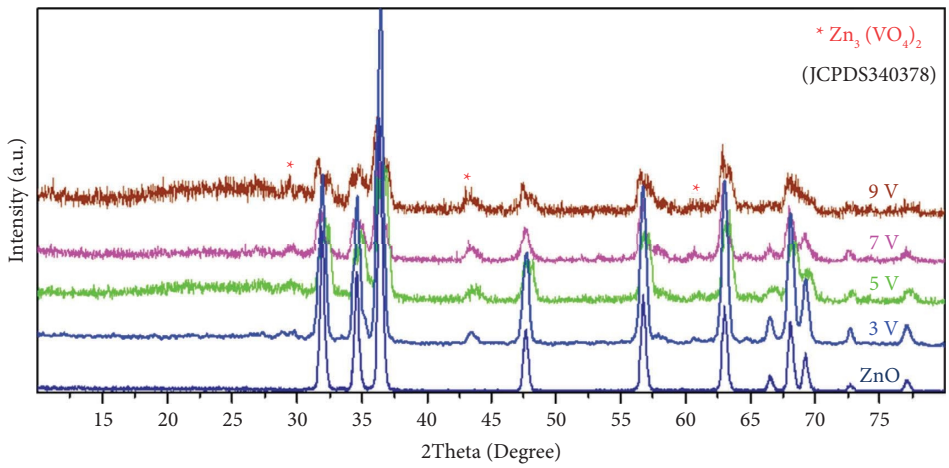

Figure 1: X-ray diffraction (XRD) pattern of the samples. The pattern of pure ZnO is given for comparison.

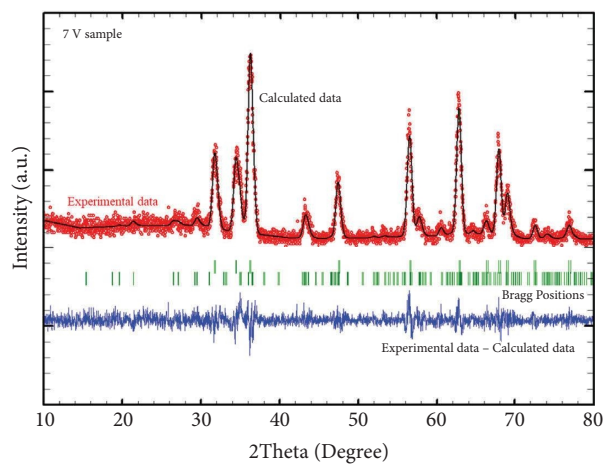

Figure 2: Rietveld refinement of the XRD pattern of 7 V sample.

Table 1: Unit cell parameters and volume determined by Rietveld refinement.

Samples	Unit cell parameters (Å)		Volume (Å^3)
	$a = b$	c	
ZnO	3.252 (4)	5.100 (1)	47.71 (1)
3 V	3.254 (8)	5.211 (1)	47.79 (2)
5 V	3.282 (1)	5.252 (2)	49.00 (3)
7 V	3.288 (4)	5.254 (3)	49.20 (3)
9 V	3.291 (5)	5.266 (1)	49.40 (2)

Furthermore, variations in bandgap values for V_2O_5/ZnO may be additionally attributed to grain size, strain, structural parameters, and composition [31, 32]. The quantum confinement effect caused by the tiny size is responsible for the blue shift in the optical bandgap.

3.3. FTIR Spectroscopy. The infrared spectra of the prepared samples are depicted in Figure 6. Symmetrical vibration of Zn-O appears to blow 500 cm^{-1} [33] (not seen here). The absorption bands detected in the other sample spectra between 750 and 950 cm^{-1} are attributable to the symmetrical and asymmetrical stretching vibrations of V = O bonds. The absorption band observed around 650 cm^{-1} corresponds to V-O-V bending vibration. The corresponding intensities increase systematically with the molar percent of V_2O_5.

3.4. SEM-EDX Analysis. Figure 7 shows SEM images of the samples. V_2O_5 nano-powder morphology presented as an aggregated parallelepiped with a smooth surface. Individual particles of various shapes in the instance of ZnO nano-powder are observed. Large spheres, as well as tiny particles, were seen in 3 V, 5 V, 7 V, and 9 V. Particle aggregation occurs in all samples, which may be caused by high-temperature calcination.

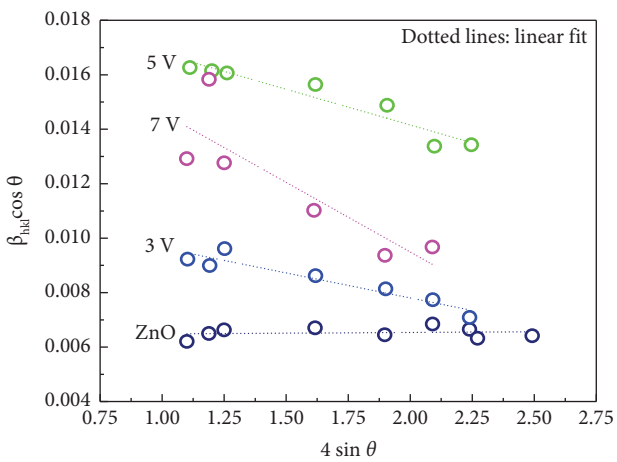

Figure 3: Williamson–Hall analyses of ZnO doped with V_2O_5.

Table 2: Crystallite size and microstrain calculated using the Debye Scherrer and Williamson–Hall methods.

Sample	Scherrer's D (nm)	Williamson–Hall analysis	
		D (nm)	ε
ZnO	21.028	21.324	0.000053
3 V	16.312	11.943	−0.00184
5 V	9.128	7.067	−0.00262
7 V	8.876	6.953	−0.00511

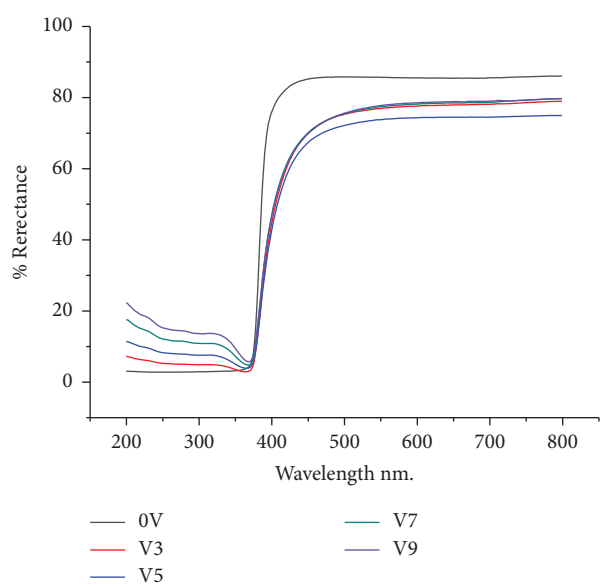

Figure 4: Diffuse reflectance spectra of the samples; 0 V, 3 V, 5 V, 7 V, and 9 V.

The EDX peaks demonstrate exclusively the elements of the samples, i.e., oxygen, vanadium, and/or zinc. For clarity, only 7 V is presented in Figure 8. As expected, the weight percent of vanadium in the samples determined by EDX is in good agreement with starting composition (Figure 8 inset table).

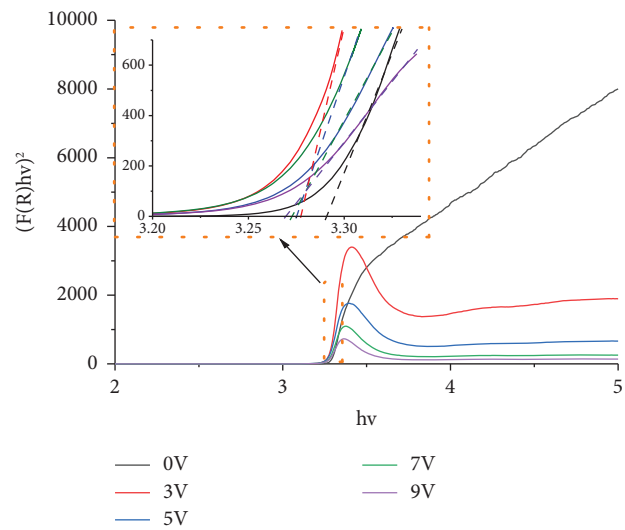

Figure 5: Tauc plot of the optical reflectance spectra of the samples; 0 V, 3 V, 5 V, 7 V, and 9 V.

Table 3: Bandgap (E_g) of the prepared materials.

Samples	E_g (eV)
ZnO	3.290
3 V	3.280
5 V	3.275
7 V	3.270
9 V	3.265

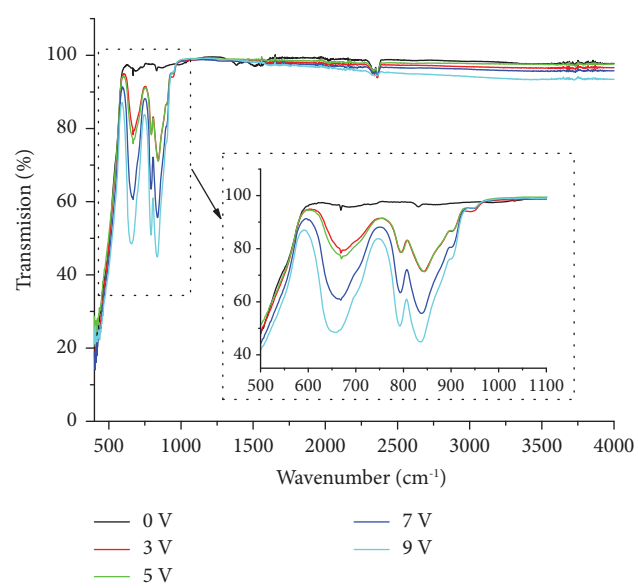

Figure 6: FTIR spectrum of the samples; 0 V, 3 V, 5 V, 7 V, and 9 V.

3.5. Photocatalytic Degradation of Methylene Blue (MB) Dye. The photocatalytic performance of the as-synthesized photocatalysts 3 V, 5 V, 7 V, and 9 V, as well as the pure ZnO, was conducted by testing MB photodegradation in an aqueous solution under visible light irradiation. In the initial stage, a blank test was performed using MB solution, with no

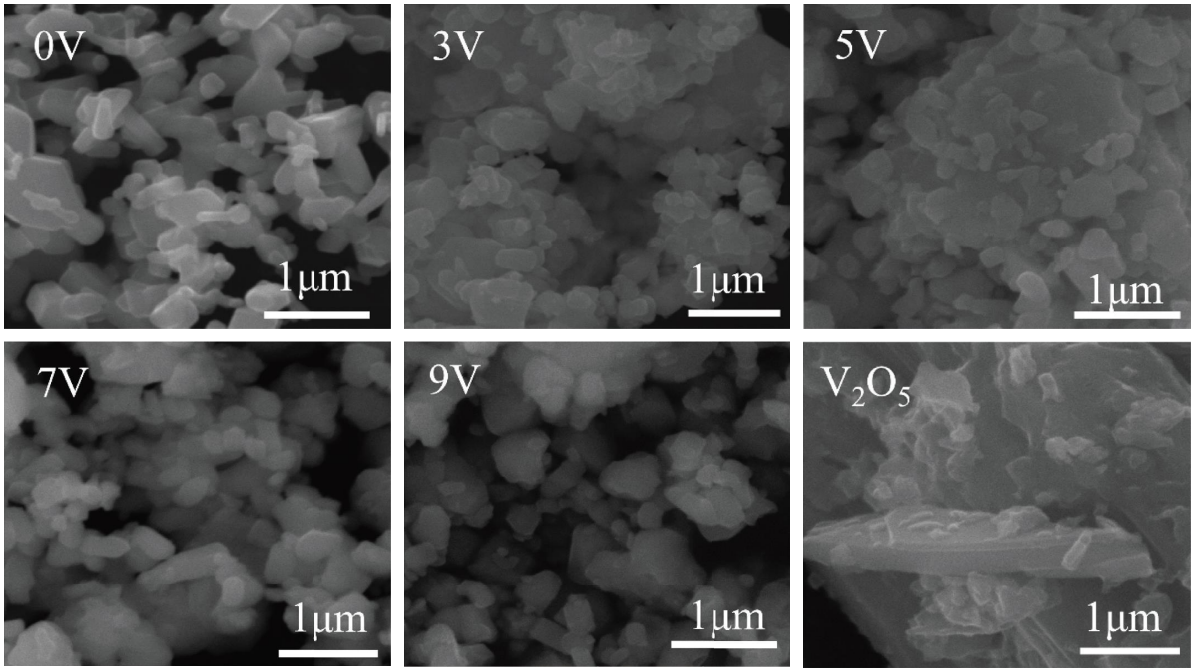

Figure 7: SEM images of the samples; 0 V (ZnO), 3 V, 5 V, 7 V, 9 V, and V_2O_5.

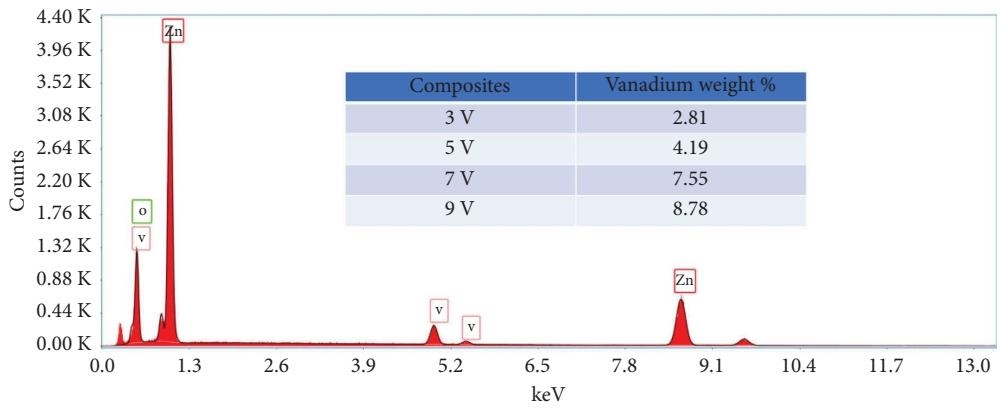

Composites	Vanadium weight %
3 V	2.81
5 V	4.19
7 V	7.55
9 V	8.78

Figure 8: The energy-dispersive X-ray spectroscopy for 7 V.

photocatalyst under visible light for 420 min. As shown in Figure 9(a), the UV-vis spectra show no change in the peak intensity of the dye (at 665 nm), suggesting that the MB cannot be effectively degraded by photolysis. In the presence of the photocatalysts, the absorption of MB dye gradually reduced with increasing irradiation time (Figure 9(b)). The photodegradation percentages of the catalysts were 70% (0 V), 37% (3 V), 82% (5 V), 90% (7 V), and 78% (9 V), after 420 min irradiation. Figure 9(c) shows the variation of C_t/C_0 of MB as a function of time under visible light irradiation in the presence of 0 V, 3 V, 5 V, 7 V, and 9 V photocatalysts. Interestingly, in the presence of the catalyst under dark conditions, the experiments indicate that after 40 min the adsorption of the dye was found to be 27% for 3 V while the other photocatalysts exhibit negligible adsorption toward dye (less than 2%). This behavior may be credited to the aggregation of V_2O_5-ZnO and the subsequently reduced surface area of the catalyst [34].

The photocatalytic degradation under visible light indicates that the ZnO doping with V_2O_5 enhances its photocatalytic performance. The best result was obtained in the presence of a 7V catalyst. These results could be attributed to the bandgap narrowing as seen from UV-vis DRS spectra. Moreover, from the XRD the particle size was found to be decreased with the increase in the V_2O_5 concentration, thus as the particle size decreases, the specific surface area increases then the photocatalytic performance increase [35, 36]. Generally, the improvement in photocatalytic activity upon V_2O_5 doping can be ascribed to the fact that the dopant species absorbs the generated electrons through irradiation and then transfers them to the oxygen molecules [34]. Doping ZnO with V_2O_5 dopant allows the separation of electron-hole pairs, thus enhancing the photocatalytic performance. Any further increase in the V_2O_5 concentration led to a decrease in the photocatalytic degradation efficiency. In link with XRD results, sample 9 V clearly shows

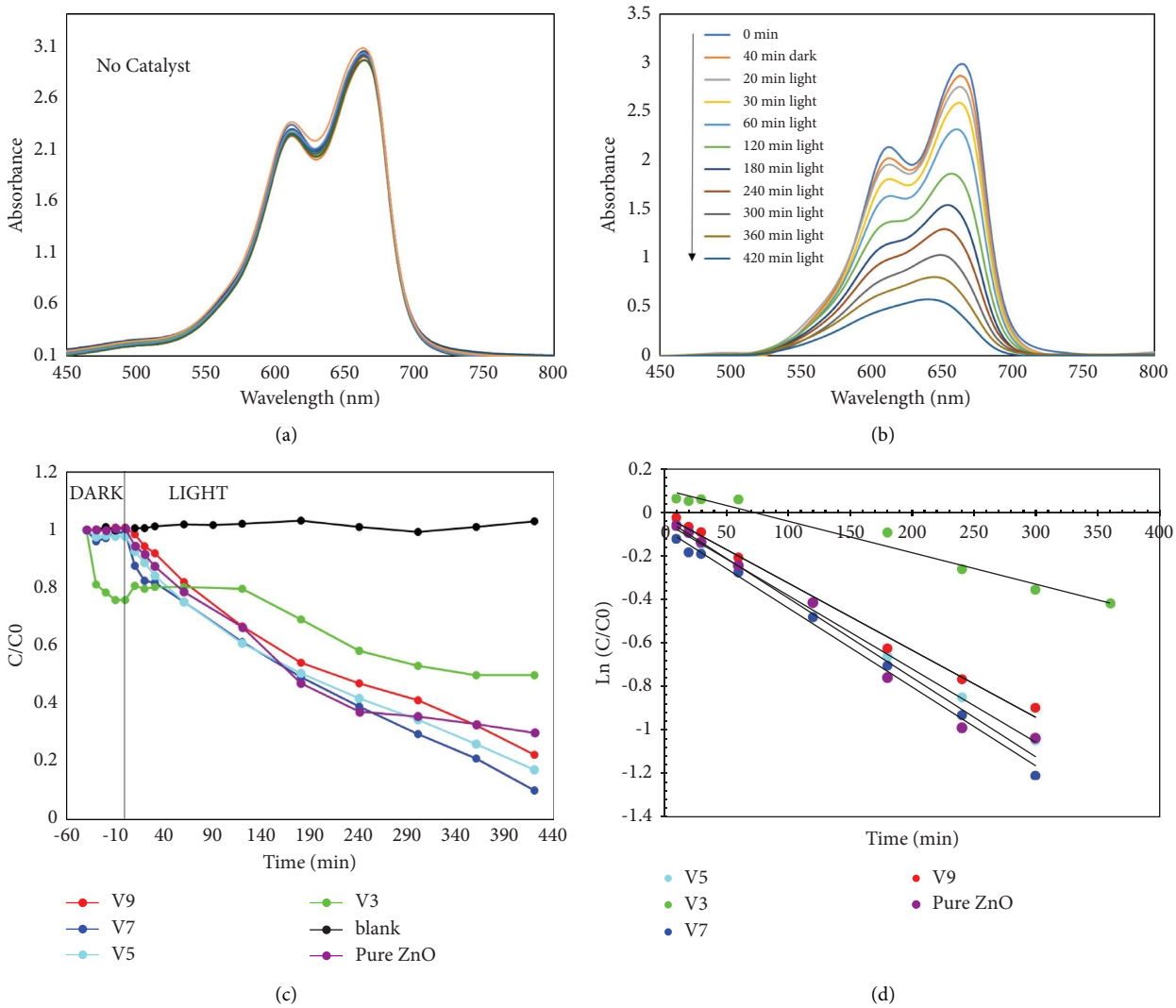

Figure 9: Photocatalytic degradation of MB over prepared materials under visible light, (a) without catalyst, (b) UV-vis spectra of MB degradation over 7 V catalyst, (c) change in the concentration of MB versus time, (d) pseudo-first-order kinetics plot of the photodegradation of MB in the presence of prepared catalysts.

the presence of $Zn_3(VO_4)_2$ as an impurity that may act as a recombination center [37]. The degradation of the MB solution under visible light irradiation was examined to fit on pseudo-first-order reaction kinetics as follows:

$$\ln\left(\frac{C_t}{C_0}\right) = k_1 t, \tag{6}$$

C_0 presents the initial concentration of the MB and C_t is the MB concentration at time $t \neq 0$. k_1 is the pseudo-first-order rate constant. The photodegradation rate constant k_1 (min^{-1}) was calculated from the slope of the straight line of $\ln(C_t/C_0)$ versus time t.

The degradation of MB over the prepared materials is best interpreted by the pseudo-first-order kinetics model (Figure 9(d)). The kinetics parameters are gathered in Table 4.

By increasing the V_2O_5 content, the initial rate increases reaching the maximum value (0.010 mmol·min^{-1}·mg^{-1}) for the 7 V catalyst then decreased when reached 9% of V_2O_5

Table 4: Pseudo-first-order kinetic parameters of MB degradation over prepared materials.

Catalyst	Pseudo-first-order k (min^{-1}) × 10^3	R^2	Degradation (%)
3 V	1.43	0.96	37
5 V	3.45	0.99	82
7 V	6.19	0.97	90
9 V	3.25	0.99	78
ZnO	3.61	0.98	70

(Figure 10). Generally, the reactive species generated during irradiation of photocatalysts are holes (h^+), hydroxyl radicals ($OH^\bullet$), and superoxide radicals ($O_2^{\bullet-}$) which mainly govern the photocatalytic mechanisms.

In the first step, a V_2O_5/ZnO photocatalyst absorbs visible light energy at an appropriate wavelength to create electron-hole pairs. During the photo-generation process, electrons are

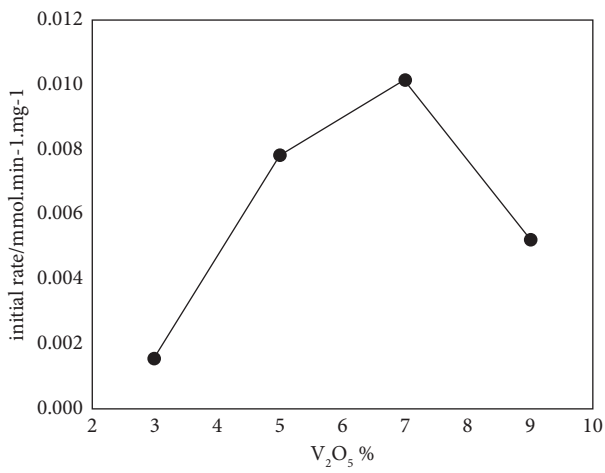

Figure 10: Change in initial rate versus the content of V_2O_5.

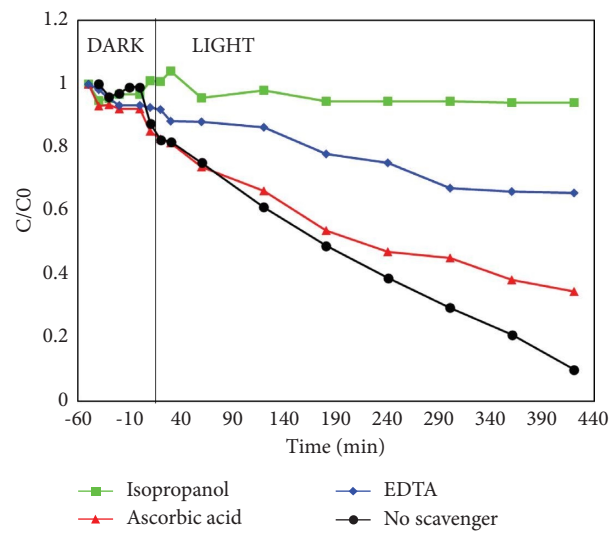

Figure 11: Effect of the presence of different scavengers on the MB degradation over prepared materials.

moved to V_2O_5, whose potential is below ZnO's conduction band. As the electrons trapped on the surface of the V_2O_5 react with the dissolved oxygen, they react with the reactive oxygen species, converting H_2O to $OH^{\bullet}$. Meanwhile, V_2O_5 enhances charge separation for photogenerated charges. As the photogenerated electrons on the ZnO surface are trapped by dissolved O_2, they cause $O_2^{\bullet-}$ to form, and then, $OH^{\bullet}$ to be formed upon their conversion into energy. Conversely, holes in the valence bond of ZnO interact with the adsorbed H_2O or hydroxyl groups to produce surface hydroxyl radicals [36].

For a better understanding of the mechanism of MB photocatalytic degradation over prepared materials, the type of reactive species that play the most significant role in photocatalytic degradation must be identified. For this purpose, these reactive species were investigated by adding (4 μmole) of different organic scavengers to the reaction medium in the presence of the catalyst. For holes (h^+) trapping, we use ethylenediaminetetraacetic acid (EDTA), isopropanol alcohol (IPA) for hydroxyl radicals ($OH^{\bullet}$), and L-ascorbic acid (ASC) for superoxide radicals ($O_2^{\bullet-}$) [38, 39]. The catalyst 7 V was used as a model catalyst in these experiments.

The effect of adding different scavengers on the photocatalytic efficiency is illustrated in Figure 11. As seen, the photocatalytic efficiency of the MB degradation over 7 V was reduced from 90% (without adding a scavenger) to 62% after adding ascorbic acid indicating that the ($O_2^{\bullet-}$) active species play a relatively minor role in the photocatalytic degradation process compared to other reactive species. On the other hand, it can be observed that after the addition of isopropanol, the photodegradation performance of MB was negligible (about 2%), while with the addition of EDTA the MB degradation was reduced by 29% compared to the catalytic performance without adding a scavenger. Therefore, the photogenerated holes in the valence band of the catalyst are trapped by H_2O molecules to give hydroxyl radicals. Hence, the photogenerated holes and hydroxyl radicals could be the most effective active species with an essential role in the photocatalytic process. Moreover, the presence of orthorhombic phase $Zn_3(VO_4)_2$ as secondary phase may act as a recombination center hole electron pair [37]. As a result, a drop of photocatalytic activity is observed for the sample 9 V containing the highest weight percentage of $Zn_3(VO_4)_2$. In addition, from Figure 9(b), we can observe that there is a blue shift of the main peak at $\lambda = 665$ nm which is shifted from 665 nm to 661 nm during the reaction. Generally, these types of blue shifts can be attributed to the different N-demethylation steps for MB degradation [40], this led us to suggest that the MB is degraded into final products in multiple steps.

3.6. Dielectric Spectroscopy. The complex impedance spectroscopic (CIS) approach is used to assess the electrical response of materials across a broad frequency and temperature range. It is the most common used approach for studying the dielectric behavior and dynamics of ionic transport in materials. In fact, this methodology is particularly beneficial in evaluating the contribution of various processes in the conduction process. As a result, the physical process occurring within the sample may be represented as an analogous circuit using impedance spectra. In Figure 12, the electrical response of the material was represented using a Nyquist diagram (spectra of the real part and the imaginary part of the complex impedance, Z^* ($Z^* = Z' + jZ''$; $j^2 = -1$), as a function of the exciting frequency). Scattered experimental points are arranged in an approximately circular arc. This response can be associated with an electric dipole formed by resistance in parallel with a capacitor. However, since the scattered points do not form exactly half circles, a model combing only resistance with a capacitor element is insufficient to describe accurately the CIS results. Hence, a Constant Phase Element (CPE) in parallel with a resistance R is usually regarded as a better representation of the circuit-fitting parameters [41]. The equivalent electrical circuit of the samples is shown in the inset of Figure 12. The red line represents the best fit.

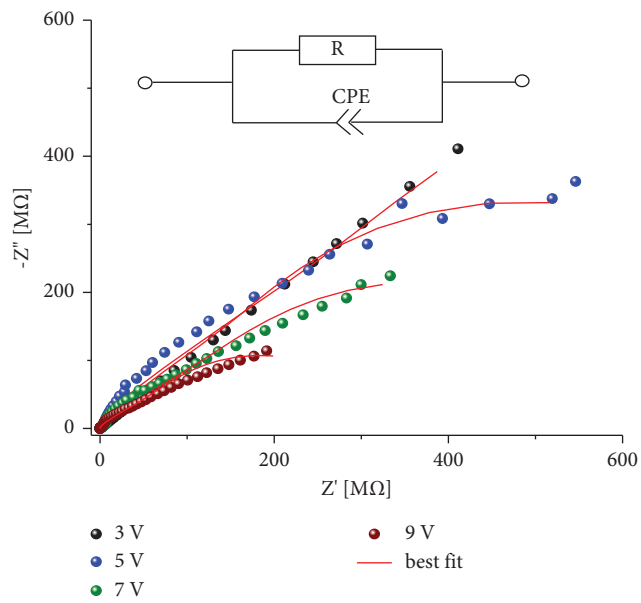

Figure 12: Nyquist plot ($-Z''$ vs. Z' plot) for the different samples; 3 V, 5 V, 7 V, and 9 V.

The total impedance of the circuit is given by

$$Z^* = \mathrm{Re}Z^* + \mathrm{Im}Z^* = Z' + jZ'' = \left(\frac{1}{R} + \frac{1}{Z^*_{\mathrm{CPE}}}\right), \quad (7)$$

where the impedance of the CPE is defined as

$$Z^*_{\mathrm{CPE}} = \frac{1}{A_0 (j\omega)^n}, \quad (8)$$

where ω is the angular frequency ($\omega = 2\pi f$), A_0 is a constant independent of frequency [42], and $0 < n < 1$ is a dimensionless parameter determining the degree of deviation from an exact semicircle [43]. When $n = 1$, equation (8) yields the impedance of a capacitor, where $A_0 = C$. The resistance R is the intercept of the impedance curve with Z' axis. The experiments have been fitted by the ORIGINLAB software based on the following relationships.

$$z' = \frac{R\left(1 + RA_0\omega^n \cos(n\pi/2)\right)}{1 + 2RA_0\omega^n \cos(n\pi/2) + \left(RA_0\omega^n\right)^2},$$
$$Z'' = \frac{R^2 A_0\omega^n \sin(n\pi/2)}{1 + 2RA_0\omega^n \cos(n\pi/2) + \left(RA_0\omega^n\right)^2}. \quad (9)$$

Figure 12 shows that increasing V_2O_5 loading induces a decrease in the capacitance C as well as the resistance R. The extracted parameters from the fit for the circuit elements are collected in Table 5.

For each loop, a time constant τ (lifetime at the depletion layer of the semiconductor) is equal to the product of the resistance and the capacitance associated with the defined loop (τ = RC). Going from 0 V to 9 V leads to a decrease in the resistance from 1547 MΩ to 321 MΩ as well as the capacitance from 14.31 pF to 2.75 pF. Accordingly, the electron lifetime decreases from 22.13 ms to 0.88 ms.

Table 5: The fitting parameters of the equivalent circuit.

Sample (V)	R (MΩ)	C (pF)	τ (ms)
3	1547	14.31	22.137
5	848.7	8.27	7.018
7	641.6	6.97	4.472
9	320.8	2.75	0.882

4. Conclusion

Vanadium oxide-doped zinc oxide samples were prepared via a solid-state reaction process. The effect of V_2O_5 on the ZnO physical properties and photocatalytic performance was reported. The XRD shows that by increasing the concentration of dopant (V_2O_5) a minor orthorhombic phase assigned to $Zn_3(VO_4)_2$ appeared at 9% of V_2O_5 and may act as a recombination center in the photocatalytic degradation of methylene blue dye. Dielectric spectroscopy analysis reveals that by increasing V_2O_5, loading the capacitance (C) decreases as well as the resistance R. The photocatalytic degradation under visible light indicates that the ZnO doping with V_2O_5 enhances its photocatalytic performance, where the best result of 90% MB degradation was obtained in the presence of 7 V catalyst.

Data Availability

The data used to support the findings of this study are included within the article.

Conflicts of Interest

The authors declare that they have no conflicts of interest.

Acknowledgments

The project was funded by the Basic and Applied Scientific Research Center, Scientific Research Deanship, and Imam Abdulrahman Bin Faisal University, KSA (2020-084-BASRC).

References

[1] D. Kelly and W. H. Weinberg, "Direct dissociative chemisorption of methane, ethane, propane, and cyclopropane on Ir(110)," *Journal of Vacuum Science and Technology A: Vacuum, Surfaces, and Films*, vol. 15, no. 3, pp. 1663–1666, 1997.

[2] E. Nurfani, A. Lailani, W. A. P. Kesuma, M. S. Anrokhi, G. T. M. Kadja, and M. Rozana, "UV sensitivity enhancement in Fe-doped ZnO films grown by ultrafast spray pyrolysis," *Optical Materials*, vol. 112, Article ID 110768, 2021.

[3] X. Liang and C. Wang, "Electron and phonon transport anisotropy of ZnO at and above room temperature," *Applied Physics Letters*, vol. 116, no. 4, Article ID 043903, 2020.

[4] M. Wraback, H. Shen, S. Liang, C. R. Gorla, and Y. Lu, "High contrast, ultrafast optically addressed ultraviolet light modulator based upon optical anisotropy in ZnO films grown on R-plane sapphire," *Applied Physics Letters*, vol. 74, no. 4, pp. 507–509, 1999.

[5] S. C. Su, H. Zhu, L. X. Zhang et al., "Low-threshold lasing action in an asymmetric double ZnO/ZnMgO quantum well structure," *Applied Physics Letters*, vol. 103, no. 13, Article ID 131104, 2013.

[6] S. J. Jiao, Z. Z. Zhang, Y. M. Lu et al., "ZnO p-n junction light-emitting diodes fabricated on sapphire substrates," *Applied Physics Letters*, vol. 88, pp. 1–3, 2006.

[7] R. Ajay Rakkesh, D. Durgalakshmi, P. Karthe, and S. Balakumar, "Anisotropic growth and strain-induced tunable optical properties of Ag–ZnO hierarchical nanostructures by a microwave synthesis method," *Materials Chemistry and Physics*, vol. 244, Article ID 122720, 2020.

[8] B. J. Jin, S. H. Bae, S. Y. Lee, and S. Im, "Effects of native defects on optical and electrical properties of ZnO prepared by pulsed laser deposition," *Materials Science and Engineering: B*, vol. 71, no. 1-3, pp. 301–305, 2000.

[9] X. Li, B. Keyes, S. Asher et al., "Hydrogen passivation effect in nitrogen-doped ZnO thin films," *Applied Physics Letters*, vol. 86, no. 12, pp. 1–3, 2005.

[10] B. J. Jin, S. Im, and S. Y. Lee, "Violet and UV luminescence emitted from ZnO thin films grown on sapphire by pulsed laser deposition," *Thin Solid Films*, vol. 366, no. 1-2, pp. 107–110, 2000.

[11] D. M. Bagnall, Y. F. Chen, M. Y. Shen, Z. Zhu, T. Goto, and T. Yao, "Room temperature excitonic stimulated emission from zinc oxide epilayers grown by plasma-assisted MBE," *Journal of Crystal Growth*, vol. 184–185, no. 1-2, pp. 605–609, 1998.

[12] I. Y. Prosanov and A. A. Politov, "Intrinsic defects and luminescence of zinc oxide," *Inorganic Materials*, vol. 31, 1995.

[13] R. Abaira, E. Buffagni, A. Matoussi, H. Khmakhem, and C. Ferrari, "Synthesis and structural properties of vanadium doped zinc oxide," *Superlattices and Microstructures*, vol. 86, pp. 438–445, 2015.

[14] S. Brahma, P. H. Lee, H. H. Chen, A. C. Lee, and J. L. Huang, "Competitive effect of dopant concentration and the size of the nanorods over the electron phonon coupling in Cd doped ZnO nanorod arrays," *Journal of Physics and Chemistry of Solids*, vol. 148, Article ID 109728, 2021.

[15] A. Sáenz-Trevizo, D. Kuchle-Mena, P. Pizá-Ruiz et al., "Microstructural and optical properties of high-quality Mg–Zn oxide thin films," *Materials Science in Semiconductor Processing*, vol. 127, Article ID 105690, 2021.

[16] Q. Fan, D. Li, J. Li, and C. Wang, "Structure and piezoelectricity properties of V-doped ZnO thin films fabricated by sol-gel method," *Journal of Alloys and Compounds*, vol. 829, Article ID 154483, 2020.

[17] Y. Q. Chen, X. J. Zheng, and X. Feng, "The fabrication of vanadium-doped ZnO piezoelectric nanofiber by electrospinning," *Nanotechnology*, vol. 21, no. 5, Article ID 055708, 2009.

[18] S. H. Shin, Y. H. Kwon, M. H. Lee, J. Y. Jung, J. H. Seol, and J. Nah, "A vanadium-doped ZnO nanosheets–polymer composite for flexible piezoelectric nanogenerators," *Nanoscale*, vol. 8, no. 3, pp. 1314–1321, 2016.

[19] J. Wang, W. Chen, and M. Wang, "Properties analysis of Mn-doped ZnO piezoelectric films," *Journal of Alloys and Compounds*, vol. 449, no. 1-2, pp. 44–47, 2008.

[20] R. Slama, J. el Ghoul, I. Ghiloufi, K. Omri, L. el Mir, and A. Houas, "Synthesis and physico-chemical studies of vanadium doped zinc oxide nanoparticles and its photocatalysis," *Journal of Materials Science: Materials in Electronics*, vol. 27, no. 8, pp. 8146–8153, 2016.

[21] S. Mrabet, N. Ihzaz, M. Alshammari et al., "Structural, optical, and magnetic properties of V-doped ZnO nanoparticles and the onset of ferromagnetic order," *Journal of Alloys and Compounds*, vol. 920, Article ID 165920, 2022.

[22] I. E. Wachs, "Catalysis science of supported vanadium oxide catalysts," *Dalton Transactions*, vol. 42, no. 33, pp. 11762–11769, 2013.

[23] S. Maensiri, C. Masingboon, V. Promarak, and S. Seraphin, "Synthesis and optical properties of nanocrystalline V-doped ZnO powders," *Optical Materials*, vol. 29, no. 12, pp. 1700–1705, 2007.

[24] J. Tauc, R. Grigorovici, and A. Vancu, "Optical properties and electronic structure of amorphous germanium," *Physica Status Solidi A*, vol. 15, no. 2, pp. 627–637, 1966.

[25] B. D. Viezbicke, S. Patel, B. E. Davis, and D. P. Birnie, "Evaluation of the Tauc method for optical absorption edge determination: ZnO thin films as a model system," *Physica Status Solidi A*, vol. 252, no. 8, pp. 1700–1710, 2015.

[26] R. Rusdi, A. A. Rahman, N. S. Mohamed, N. Kamarudin, and N. Kamarulzaman, "Preparation and band gap energies of ZnO nanotubes, nanorods and spherical nanostructures," *Powder Technology*, vol. 210, no. 1, pp. 18–22, 2011.

[27] M. Nowak, B. Kauch, and P. Szperlich, "Determination of energy band gap of nanocrystalline SbSI using diffuse reflectance spectroscopy," *Review of Scientific Instruments*, vol. 80, no. 4, Article ID 046107, 2009.

[28] R. López and R. Gómez, "Band-gap energy estimation from diffuse reflectance measurements on sol-gel and commercial TiO 2: a comparative study," *Journal of Sol-Gel Science and Technology*, vol. 61, pp. 1–7, 2012.

[29] N. Sangiorgi, L. Aversa, R. Tatti, R. Verucchi, and A. Sanson, "Spectrophotometric method for optical band gap and electronic transitions determination of semiconductor materials," *Optical Materials*, vol. 64, pp. 18–25, 2017.

[30] R. Abaira, T. Dammak, A. Matoussi, and A. Younes, "Structural and optical properties of zinc oxide doped by V2O5 synthesized by solid-state reaction," *Superlattices and Microstructures*, vol. 91, pp. 365–374, 2016.

[31] N. Goswami and A. Sahai, "Structural transformation in nickel doped zinc oxide nanostructures," *Materials Research Bulletin*, vol. 48, no. 2, pp. 346–351, 2013.

[32] J. Zhao, L. Wang, X. Yan et al., "Structure and photocatalytic activity of Ni-doped ZnO nanorods," *Materials Research Bulletin*, vol. 46, no. 8, pp. 1207–1210, 2011.

[33] R. Wahab, S. G. Ansari, Y. S. Kim, M. A. Dar, and H.-S. Shin, "Synthesis and characterization of hydrozincite and its conversion into zinc oxide nanoparticles," *Journal of Alloys and Compounds*, vol. 461, no. 1-2, pp. 66–71, 2008.

[34] W. Raza, M. M. Haque, M. Muneer, and D. Bahnemann, "Synthesis of visible light driven TiO2 coated carbon nanospheres for degradation of dyes," *Arabian Journal of Chemistry*, vol. 12, no. 8, pp. 3534–3545, 2019.

[35] C. Retamoso, N. Escalona, M. González et al., "Effect of particle size on the photocatalytic activity of modified rutile sand (TiO2) for the discoloration of methylene blue in water," *Journal of Photochemistry and Photobiology A: Chemistry*, vol. 378, pp. 136–141, 2019.

[36] H. A. Kiwaan, T. M. Atwee, E. A. Azab, and A. A. El-Bindary, "Efficient photocatalytic degradation of Acid Red 57 using synthesized ZnO nanowires," *Journal of the Chinese Chemical Society*, vol. 66, no. 1, pp. 89–98, 2019.

[37] J. Z. Marinho, L. F. de Paula, E. Longo, A. O. T. Patrocinio, and R. C. Lima, "Effect of Gd3+ doping on structural and photocatalytic properties of ZnO obtained by facile

microwave-hydrothermal method," *SN Applied Sciences*, vol. 1, no. 4, pp. 359–413, 2019.

[38] C. Zheng, H. M. Cao, Z. Liu, T. Liu, and S. Duo, "Limited space assembly of 2,5-dihdroxy-1,4-benzenedicarboxylic acid-modified ZnO plane-like flowers via synergistic effect of carboxyl, phenyl, and hydroxyl groups and their morphology-related photocatalytic property," *Journal of Materials Science: Materials in Electronics*, vol. 31, no. 22, pp. 19819–19835, 2020.

[39] N. Khadgi, A. R. Upreti, and Y. Li, "Simultaneous bacterial inactivation and degradation of an emerging pollutant under visible light by ZnFe 2 O 4 co-modified with Ag and rGO," *RSC Advances*, vol. 7, no. 43, pp. 27007–27016, 2017.

[40] D. D. Mishra and G. Tan, "Visible photocatalytic degradation of methylene blue on magnetic SrFe12O19," *Journal of Physics and Chemistry of Solids*, vol. 123, pp. 157–161, 2018.

[41] M. E. Guzhva, V. V. Lemanov, P. A. Markovin, and W. Kleemann, "Critical concentrations in Ba-doped incipient ferroelectric SrTiO3," *Physics of the Solid State*, vol. 39, no. 4, pp. 618–624, 1997.

[42] J. B. Jorcin, M. E. Orazem, N. Pébère, and B. Tribollet, "CPE analysis by local electrochemical impedance spectroscopy," *Electrochimica Acta*, vol. 51, no. 8-9, pp. 1473–1479, 2006.

[43] C. Bouzidi, N. Sdiri, A. Boukhachem, H. Elhouichet, and M. Férid, "Impedance analysis of BaMo1−xWxO4 ceramics," *Superlattices and Microstructures*, vol. 82, pp. 559–573, 2015.